Inorganic Chemistry

Article

pubs.acs.org/IC

Molecular Structures and Solvation of Free Monomeric and Dimeric Ferriheme in Aqueous Solution: Insights from Molecular Dynamics Simulations and Extended X-ray Absorption Fine Structure Spectroscopy

David Kuter,[†,‡] Victor Streltsov,[§] Natalia Davydova,[§] Gerhard A. Venter,[†,‡] Kevin J. Naidoo,*[,†,‡] and Timothy J. Egan*[,†]

[‡]Scientific Computing Research Unit, [†]Department of Chemistry, University of Cape Town, Private Bag, Rondebosch 7701, South Africa

[§]Manufacturing Flagship, CSIRO, Parkville, Victoria 3050, Australia

Ⓢ *Supporting Information*

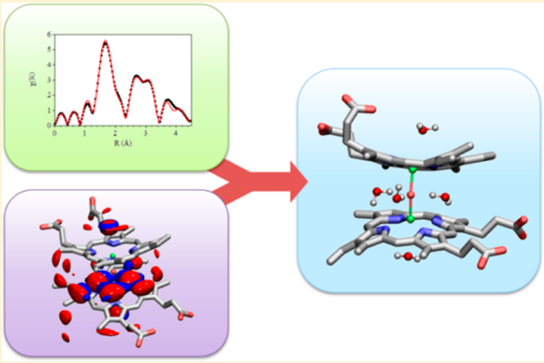

ABSTRACT: CHARMM force field parameters have been developed to model nonprotein bound five-coordinate ferriheme (ferriprotoporphyrin IX) species in aqueous solution. Structures and solvation were determined from molecular dynamics (MD) simulations at 298 K of monomeric [HO-ferriheme]$^{2-}$, [H_2O-ferriheme]$^{-}$, and [H_2O-ferriheme]^{0}; $\pi-\pi$ dimeric [(HO-ferriheme)$_2$]$^{4-}$, [(H_2O-ferriheme)(HO-ferriheme)]$^{3-}$, [(H_2O-ferriheme)$_2$]$^{2-}$, and [(H_2O-ferriheme)$_2$]^{0}; and μ-oxo dimeric [μ-(ferriheme)$_2$O]$^{4-}$. Solvation of monomeric species predominated around the axial ligand, meso-hydrogen atoms of the porphyrin ring (H_{meso}), and the unligated face. Existence of $\pi-\pi$ ferriheme dimers in aqueous solution was supported by MD calculations where such dimers remained associated over the course of the simulation. Porphyrin rings were essentially coplanar. In these dimers major and minor solvation was observed around the axial ligand and H_{meso} positions, respectively. In μ-oxo ferriheme, strong solvation of the unligated face and bridging oxide ligand was observed. The solution structure of the μ-oxo dimer was investigated using extended X-ray absorption fine structure (EXAFS) spectroscopy. The EXAFS spectrum obtained from frozen solution was markedly different from that recorded on dried μ-oxo ferriheme solid. Inclusion of five solvent molecules obtained from spatial distribution functions in the structure generated from MD simulation was required to produce acceptable fits to the EXAFS spectra of the dimer in solution, while the solid was suitably fitted using the crystal structure of μ-oxo ferriheme dimethyl ester which included no solvent molecules.

■ INTRODUCTION

Nonprotein bound (free) ferriheme (ferriprotoporphyrin IX) plays important roles in biological systems.[1] It is an inducer of differentiation in various cell types including mouse neuroblastoma,[2] 3T3,[3] and leukemic cells[4] as well as human hematopoietic[5] and leukemic cells.[6] It has also been implicated as a regulator of gene expression.[7] On the other hand, high cellular concentrations of free ferriheme are known to generate damaging reactive oxygen species.[8,9] Moreover, its propensity to accumulate and aggregate in lipid membranes causes increased membrane disorder and enhanced permeability which can lead to cell lysis and death.[10,11] Such effects often occur as a result of severe hemolysis, for example, after hemorrhagic stroke[12] or during diseases such as sickle cell anemia[13] or malaria.[14] Furthermore, release of ferriheme from hemoproteins has been implicated in conditions such as inflammation, atherogenesis, cancer, and Alzheimer's disease.[15−19]

Early studies proposed that the dominant form of free ferriheme in aqueous solution is a μ-oxo dimer.[20] Despite subsequent contradictory evidence,[21] this notion persisted for several decades, albeit with uncertainty regarding the extent of its aggregation and stability.[22−28] Recently, it has been shown that the dominant species is in fact a $\pi-\pi$ dimer.[29−31] Induction of μ-oxo ferriheme from the $\pi-\pi$ dimeric species is possible by inclusion of aprotic water-miscible organic solvents at high pH;[30] high salt concentrations in aqueous solution;[30] or by the addition of the antimalarial drug chloroquine.[32,33]

On the other hand, little is known about the solution structures or solvation of the various ferriheme species. Molecular dynamics (MD) simulations are well suited to address this, but they are heavily reliant on the quality of the force field. In this study the CHARMM molecular modeling

Received: February 26, 2014
Published: October 2, 2014

Scheme 1

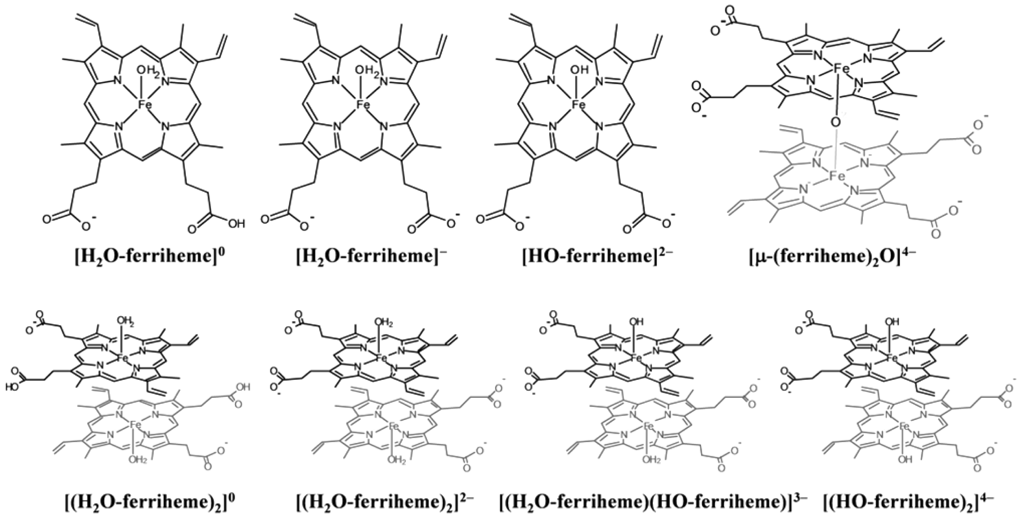

software package was used.[34] The CHARMM36 force field contains parameters for ferrous heme, but not for the ferric form. Ferriheme models for use with CHARMM have been previously reported by Autenrieth et al.[35] but were developed specifically for six-coordinate ferriheme for use in hemoproteins and thus are not optimal for studying five-coordinate ferriheme species in aqueous solution. To date, no five-coordinate ferriheme models applicable to the unbound state have been established for use in CHARMM.

Here we present free ferriheme models parametrized for use with the CHARMM force field. These include monomeric [H_2O-ferriheme]^0, [H_2O-ferriheme]$^-$, and [HO-ferriheme]$^{2-}$ as well as dimeric [μ-(ferriheme)$_2$O]$^{4-}$ (see Scheme 1). MD simulations of monomeric, $\pi-\pi$ dimeric (see Scheme 1, bottom row) and μ-oxo ferriheme species in aqueous solution were performed using the TIP4P-Ew water model.[36] Solvation of ferriheme species was probed using spatial distribution functions (SDFs) and dynamic structure and orientation of dimeric ferriheme species is reported. Experimental extended X-ray absorption fine structure (EXAFS) spectroscopy was performed on a frozen solution of the Na^+ salt of [μ-(ferriheme)$_2$O]$^{4-}$ which was fitted using structural data obtained from MD simulations.

■ EXPERIMENTAL SECTION

All chemicals were purchased from Sigma-Aldrich, except for hemin (Fluka) and D_2O (Merck). Magnetic susceptibility measurements were made on a Bruker Ultrashield 400 Plus NMR spectrometer using the Evans method as described previously.[37] The magnetic moment of ferriheme was determined in three different solutions. The first contained hematin (3 mg) in 1.2 mL of NaOD (1.67 mM) and 0.8 mL poly(ethylene glycol) 400 (PEG400). The second consisted of hematin (3 mg) in 1.35 mL of NaOD (26 mM) and 0.4 mL of PEG400 which was pD adjusted to 7.4 using 50 μL phosphoric acid (0.1 M) and made up to 2 mL with D_2O. The third consisted of hematin (3 mg) in 2 mL of CD_3OD which contained 58 mM NaOD. Reference solutions were prepared as described for sample solutions but excluded ferriheme.

Solid Na_4[μ-(ferriheme)$_2$O] was prepared as reported previously.[33] The solution sample of [μ-(ferriheme)$_2$O]$^{4-}$ for EXAFS measurements was prepared by diluting 0.25 mL of a stock hemin solution (20 mM in 0.1 M NaOH) in 0.2 mL of PEG400, 0.4 mL of DMSO, and 0.1 mL of aqueous *N*-cyclohexyl-2-aminoethanesulfonic acid (CHES, 0.2 M, pH 10). This was adjusted to pH 10 using 1 M $HClO_4$, and water was added to a final volume of 1 mL. The cryoprotectant PEG400 produced stable solutions, unlike glycerol which caused ferriheme to precipitate. EXAFS data were acquired at the Australian synchrotron XAS beamline (1.9 T Wiggler). The solution sample was injected into 0.1 mL Teflon cells (DuPont, Wilmington, Delaware) made with two Kapton windows (Goodfellow Cambridge, Cambridge, UK) and rapidly frozen in liquid nitrogen. The powder sample was placed between two Kapton tapes and attached to Teflon cells. For each sample a series of four Fe Kα edge (E_0 = 7112 eV) X-ray absorption spectrum scans up to k = 12 Å^{-1} were obtained in fluorescence mode using a 100-element liquid N_2-cooled Ge detector, either at ambient temperature for solid samples or at ~15 K for liquid samples using a helium displex cryostat. Each scan was collected at a different sample spot to monitor radiation damage, which was also tested by quick XANES measurement in the 30 min exposure intervals. The incident X-ray intensity was monitored using an ionization chamber. The stability of the monochromator energy was checked for all spectra by simultaneous accumulation of an Fe foil spectrum by transmittance. This was also used for energy calibration and alignment of the EXAFS scans of the sample.

EXAFS oscillations $\chi(k)$ were extracted from experimentally measured absorption coefficients using an automated background subtraction AUTOBK algorithm implemented in the program ATHENA (v0.8.061).[38] These oscillations were quantitatively analyzed by the ARTEMIS program (v0.8.014),[38] also an interface to IFEFFIT,[39] using ab initio theoretical amplitude, phase, and mean-free path factors calculated by FEFF8.4.[40] Data were Fourier transformed from $\chi(k)$ to $\chi(R)$ choosing k-space ranges where values approached zero at both ends. This ensured that Fourier transformation termination errors (FT ringing) were negligible, thus obviating the need for use of a window function. To increase the degree of determinacy of the model, the number of variable fitting parameters was minimized by using a constrained and restrained refinement procedure. This procedure consisted of successive cycles of restrained simultaneous refinement with k^1, k^2, and k^3-weights of $\chi(k)$ data in k-space ($2.4 \leq k \leq 9.8$ Å^{-1} for the liquid sample, $2.3 \leq k \leq 12$ Å^{-1} for the solid sample), followed by refinement with k^3 in R-space ($1 \leq R \leq 4.3$ Å for the liquid sample, $1 \leq R \leq 4.4$ Å for the solid sample). Multiple scattering (MS) contributions >10% and triple scattering paths with four legs were included in the refined model. The amplitude reduction (core-hole) factor, S_0^2, and the photoelectron energy threshold adjustment parameter, ΔE_0, were refined for each data set. The data sets were averaged by the measurement uncertainties, ε_k, in k-space. The values of R-factor and χ^2 (reduced goodness-of-fit) were calculated in R-space.[39,41] The final step of refinement was conducted with weighting factors of 100 and 1000 for solid and solution state spectra, respectively.

Table 1. Water Interaction Energies (kcal mol^{-1}) for Monomeric Ferriheme Species Calculated Using Optimized Atomic Charges in CHARMM and Using DFT (OPBE/6-31G*)

		water interaction energy					
		$[H_2O\text{-ferriheme}]^{0b}$		$[H_2O\text{-ferriheme}]^{-c}$		$[HO\text{-Ferriheme}]^{2-c}$	
	interaction type^a	QM	CHARMM	QM	CHARMM	QM	CHARMM
1	$COO^-\cdots H{-}OH$	−7.1	−6.3	−10.0	−9.6	−15.6	−13.1
2	$COOH\cdots OH_2$	−7.3	−6.8	–^{d}	–^{d}	–^{d}	–^{d}
3	$C{=}O\cdots H{-}OH$	−4.6	−5.0	–^{d}	–^{d}	–^{d}	–^{d}
4	$H_{meso}\cdots OH_2$	spin contaminated		−2.9	−3.8	spin contaminated	
5	$H_{meso}\cdots OH_2$	−2.8	−3.1	−0.7	−1.0	spin contaminated	
6	$H_{meso}\cdots OH_2$	−2.8	−2.6	−0.7	−1.5	0.9	0.8
7	$H_{meso}\cdots OH_2$	−1.2	−1.0	0.7	0.6	2.0	2.5
8	$H_{vinyl}\cdots OH_2$	−2.2	−2.8	−0.7	−1.7	−0.7	0.3
9	$H_{vinyl}\cdots OH_2$	−1.7	−1.4	−0.2	−0.1	0.9	1.4
10	$O{-}H_{ax}\cdots OH_2$	−10.9	−10.2	−6.6	−7.3	−1.9	−1.6
11	$O_{ax}\cdots H{-}OH$	−2.4	−1.8	−2.4	−3.7	−8.1	−8.9
12	$N\cdots H{-}OH$	−2.3	−3.4	−2.7	−3.9	−3.1	−4.5
13	$Fe\cdots OH_2$	−3.4	−4.2	−2.2	−3.3	2.6	1.4
	MUE	0.5		0.7		0.9	

^{a}See Supporting Information Figure S2 for numbering. ^{b}QM interaction energy scaled by 1.07 × 1.16 = 1.24. ^{c}QM interaction energy scaled by 1.07. ^{d}Not applicable. MUE = mean unsigned error.

The EXAFS spectrum of the solid sample was fitted using the crystal structure of μ-oxo ferriheme dimethyl ester as input geometry.[42] Six first and six second order cumulants, ΔR and σ^2, describing the oxide bridge (O_{oxo}), pyrrole N, C_α, C_β, C_{meso}, and Fe atoms were treated as variables in the fitting procedure. As suggested by Hudson et al.,[43] second order cumulants for collinear MS paths can be described by $q \times \sigma^2$, where q ranges between 0 and 4. Consequently, collinear MS paths $Fe{-}O_{oxo}$ and $O_{oxo}{-}Fe{-}O_{oxo}$ were both described by $4 \times \sigma_{oxo}{}^2$.

The MD structure used for SDF calculations (see Computational Details, below) was employed as the initial geometry in fitting of the EXAFS spectrum of the frozen solution sample. Initial solvent atom positions were taken from positions of highest probability in the SDF. MD simulation data were used to estimate ΔR and σ^2 values according to eqs 1 and 2:[44,45]

$$\Delta R_i = \alpha \times R_{i,\mathrm{ave}} \qquad (1)$$

$$\sigma_i^2 = \beta \times \langle (R_{i,\mathrm{ave}} - R_i)^2 \rangle \qquad (2)$$

where α and β are adjustable scale factors, i is the ith scattering atom, R_i is the distance of the scattering atom from Fe, and $R_{i,\mathrm{ave}}$ is the average R_i. The parameters R_i and $R_{i,\mathrm{ave}}$ were calculated from 200 000 structures obtained from a 10 ns MD simulation. Initial values of $R_{i,\mathrm{ave}}$ and $\langle (R_{i,\mathrm{ave}} - R_i)^2 \rangle$ determined from the simulation are given in Supporting Information Table S1.

■ COMPUTATIONAL DETAILS

Parametrization. The CHARMM potential energy function, $U(\vec{R})$, is given by eq 3 and is the sum over bonded and nonbonded interactions.[34] The former include bond (b), angle (θ), Urey−Bradley (UB, S), dihedral angle (ϕ), and improper angle (ω) terms. Parameterization requires optimization of force constants (K_b, K_θ, K_{UB}, K_ϕ, and K_ω) and reference bonds/angles (b_0, θ_0, S_0, ϕ, and ω_0). In the case of dihedral angles, additional parameters include n and δ which are the periodicity and phase shift, respectively. Nonbonded interactions between atoms i and j are described by van der Waals (Lennard-Jones 6−12) and electrostatic Coulomb potential functions. In the case of the former, $\varepsilon_{i,j}{}^{\min}$, $R_{\min}$, and $r_{i,j}$ represent the well depth, position of the function minimum, and distance, respectively, while in the latter ε_0, ε, and $q_{i,j}$ are the permittivity of vacuum, relative dielectric constant (1 in explicit solvent), and atomic charges on atoms i and j, respectively.

$$\begin{aligned} U(\vec{R}) = {} & \sum_{\text{bonds}} K_b(b - b_0)^2 + \sum_{\text{angles}} K_\theta(\theta - \theta_0)^2 \\ & + \sum_{\text{Urey−Bradley}} K_{UB}(S - S_0)^2 + \sum_{\text{dihedrals}} K_\Phi(1 + \cos(n\Phi - \delta)) \\ & + \sum_{\substack{\text{improper}\\\text{dihedrals}}} K_\omega(\omega - \omega_0)^2 + \sum_{\text{non−bonded}} \left\{ \left(\frac{q_i q_j}{4\pi\varepsilon_0 r_{ij}} \right) \right. \\ & \left. + \varepsilon_{ij}^{\min} \left[\left(\frac{R_{\min,ij}}{r_{ij}} \right)^{12} - 2 \left(\frac{R_{\min,ij}}{r_{ij}} \right)^{6} \right] \right\} \end{aligned} \qquad (3)$$

Structures of monomeric $[HO\text{-ferriheme}]^{2-}$, $[H_2O\text{-ferriheme}]^-$, $[H_2O\text{-ferriheme}]^0$, and dimeric $[\mu\text{-(ferriheme)}_2O]^{4-}$ were parametrized for use in molecular mechanics (MM) simulations. Selected reference values, b_0 and θ_0, as well as selected K_θ force constants (eq 3) were adjusted until MM-minimized geometries agreed with structures determined using density functional theory (DFT) as well as crystallographic data from the Cambridge Structural Database (CSD)[46] for related iron(III) porphyrins. DFT calculations employed the OPBE and LANL2DZ basis set combination (OPBE/LANL2DZ) owing to its ability to reproduce structures of $[H_2O\text{-ferriheme}]^{+/0/-}$ and $[\mu\text{-(ferriheme)}_2O]^{4-}$ species.[37] $[H_2O\text{-ferriheme}]^{0/-}$ and $[\mu\text{-(ferriheme)}_2O]^{4-}$ were both modeled in the high-spin ($S = {}^5/_2$) state based on prior evidence.[37] For $[\mu\text{-(ferriheme)}_2O]^{4-}$, broken symmetry was used to describe antiferromagnetic coupling. The magnetic susceptibility of $[HO\text{-ferriheme}]^{2-}$ was measured and found to be 4.34 μ_B, indicating an admixed high- ($S = {}^5/_2$) and intermediate-spin ($S = {}^3/_2$) state. DFT calculations performed for both spin states produced optimized geometries showing only minor differences (see Supporting Information Table S2). The high-spin state geometry was used for parametrization because it was lower in energy (∼9 kcal mol^{-1}) and showed better agreement with related iron(III) porphyrin crystal structures. It should be noted that $[HO\text{-ferriheme}]^{2-}$ and $[\mu\text{-(ferriheme)}_2O]^{4-}$ displayed instability with respect to electron detachment in vacuum but were stable if computed with an implicit water model. The ferriheme moiety was created by duplicating the HEME residue in CHARMM and replacing the iron center with a new atom type (see Supporting Information Figure S1). Four new atom types were used to describe oxygen and hydrogen atoms of water and hydroxide ligands, respectively, and a fifth the oxygen atom of the oxide ligand. Nonbonded Lennard-Jones parameters for new hydrogen and oxygen atom types were taken from the corresponding atoms describing TIP3P water, while those for the new iron atom type were taken from de Hatten et al.[47]

Atomic charges were parametrized so as to maximize agreement between MM- and quantum mechanically- (QM) derived electrostatic surface potentials (ESPs) in vacuum and, in the case of ferriheme monomers, interaction energies between selected porphyrin atoms and a test water molecule (water interaction energies). MM ESPs generated for visualization were calculated using a method previously reported.[48] The FitCharge module in CHARMM was used to fit MM atomic charges to the QM molecular electrostatic potentials generated using the Merz−Kollman scheme in Gaussian09.[49] Fits were restrained to reproduce the QM dipole. Initial atomic charges for the three monomeric ferriheme species were determined by averaging Mulliken charges of equivalent atom types. Excess charge was summed into the axial oxygen atom. In accordance with CHARMM methodology,[34] all aliphatic hydrogen atoms were set to a value of 0.09e and excess charge summed into the attached carbon atom. The CHARMM parametrization protocol calls for HF/6-31G* to be used when calculating water interaction energies; however, this method produced substantial spin-contamination for ferriheme species. Therefore, OPBE/6-31G* was used and produced usable interaction energies in the case of monomeric species for most of the selected atoms (see Table 1 and Supporting Information Figure S2). To retain compatibility with the normal CHARMM parametrization methodology, a factor of 1.07 was used to scale OPBE/6-31G* interaction energies. This was the value found to scale the interaction energy of a water dimer calculated using OPBE/6-31G* to the same energy obtained using HF/6-31G*. Interaction energies were scaled by a further factor of 1.16 for $[H_2O\text{-ferriheme}]^0$ as recommended for neutral molecules in CHARMM. MM atomic charges of monomeric species were altered iteratively using both water interaction energies and ESP fitting until satisfactory agreement was obtained. In the case of $[\mu\text{-(ferriheme)}_2O]^{4-}$, water interaction energies could not be determined owing to the persistence of significant spin contamination despite using OPBE/6-31G*. Consequently, atomic charges for this molecule were optimized based solely on the QM ESP. To aid this, initial atomic charges for $[\mu\text{-(ferriheme)}_2O]^{4-}$ were calculated using a ratiometric approach by dividing the optimized MM charge for each atom type of $[HO\text{-ferriheme}]^{2-}$ by its Mulliken charge determined from DFT calculation, followed by multiplication with the Mulliken charge of equivalent or near equivalent atoms of the μ-oxo dimer.

The nonprotein bound five-coordinate ferriheme force field can be downloaded from http://www.scientificcomputing.com.

MD Simulations. The CHARMM software package (version 35) was employed for all MD simulations using the TIP4P-Ew water model. Ferriheme species were placed in the center of a cubic water box of length 55 Å and appropriately neutralized by Na^+ ions when required. One, two, three, or four ions were initially positioned near box corners to minimize their interaction with the ferriheme molecules (unfavorable Na^+-Na^+ interactions were negligible after equilibration of the system). Energy minimization (steepest decent for 100 and conjugate gradient for 200 steps) and system equilibration at 298 K under isobaric−isothermal ensemble (NPT) for 2 ns followed. The average box length over the last 200 ps of the NPT equilibration was determined and used in subsequent canonical ensemble (NVT) simulations. These involved 2 ns equilibration, followed by 10 ns of production dynamics. In both NPT and NVT simulations, periodic boundary conditions were employed and trajectories integrated using the Leapfrog Verlet algorithm with a 1 fs time step. Electrostatic interactions were calculated using particle-mesh Ewald with a 16.0 Å real space cutoff and grid size of approximately 1 Å. Lennard-Jones interactions were decreased smoothly to zero between 12.0 and 14.0 Å using an atom-based switching function. A Nosé−Hoover thermostat and a Langevin piston barostat were used to maintain temperature and pressure, respectively.[50−52]

SDFs were calculated as previously reported where the distribution of water molecules relative to the ferriheme coordinate frame was determined.[48,53−55] For monomeric species and $[\mu\text{-(ferriheme)}_2O]^{4-}$, the frame with lowest root mean squared deviation from the average structure was used as reference coordinate for orientation. In the case of $\pi-\pi$ dimers, a cluster analysis was performed in CHARMM using the dihedral described by the meso carbon atom between propionate side chains and the iron center of the two ferriheme molecules. The frame situated closest to the center of the cluster with the largest population was used as the reference coordinate. Porphyrin orientation analysis was performed by determining the least-squares plane (LSP) through iron and porphine structures of porphyrin rings A and B. Thereafter the entire molecule was transposed so that the LSP of porphyrin A (LSP_A) lay in the x,y-plane. Vertical interplanar distance between LSP_A and LSP_B was then simply defined as the Z-component of LSP_B. Lateral shifts were computed by projecting the center of mass of LSP_A onto LSP_B and measuring its distance from the center of mass of LSP_B. The interplanar angle α was calculated using eq 4:

$$\alpha = \cos^{-1}\frac{N_A \cdot N_B}{n_A \times n_B} \tag{4}$$

where the numerator is the dot product of the vectors normal to each LSP (N_A and N_B) and the denominator the product of the magnitude of these vectors (n_A and n_B). Dihedral angles between porphyrins were determined by calculating the angles between lines on each LSP joining the meso carbon atoms situated between the propionate side chains of each porphyrin to the center of mass of each LSP.

■ RESULTS

Parametrization. MM atomic charges for monomeric ferriheme species were optimized so as to maximize resemblance of MM and QM ESPs in vacuum (see Figure 1a−e) and reproduce QM water interaction energies to better than 1 kcal mol^{-1} (see Table 1). The best agreement was obtained for $[H_2O\text{-ferriheme}]^0$ where the mean unsigned error (MUE) in water interaction energies was 0.5 kcal mol^{-1} with only the N···H−OH interaction deviating by more than 1 kcal mol^{-1}. In the case of $[H_2O\text{-ferriheme}]^-$, the MUE was only marginally larger (0.7 kcal mol^{-1}). Agreement for the $[HO\text{-ferriheme}]^{2-}$ species was not quite as good. The MUE was 0.9

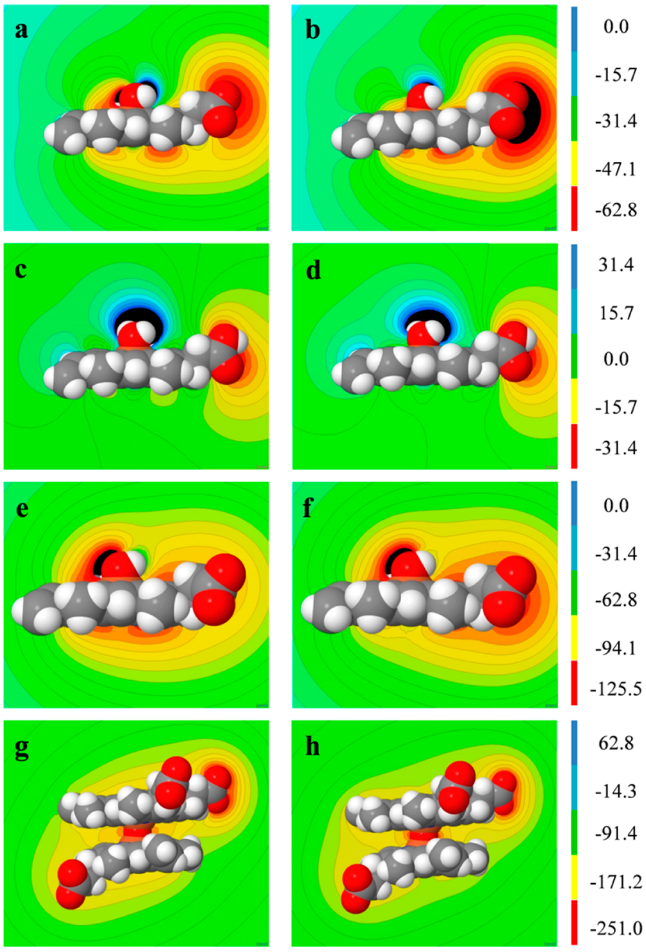

Figure 1. QM- (left) and MM-generated ESPs (right) of ferriheme species. (a, b) $[H_2O\text{-ferriheme}]^-$; (c, d) $[H_2O\text{-ferriheme}]^0$; (e, f) $[HO\text{-ferriheme}]^{2-}$; (g, h) $[\mu\text{-(ferriheme)}_2O]^{4-}$. ESPs were visualized using the Jmol software package. Energies displayed are in kcal mol^{-1}.

kcal mol^{-1}, and the fitted MM ESP (Figure 1f) revealed small qualitative differences from the QM ESP (Figure 1e). Regions close to the van der Waals radius of propionate side chain atoms exhibited greater negative potential, while those near the unligated face of the porphyrin ring showed less negative potential in the MM model. Attempts to adjust atomic charges to better resemble the QM ESP (see Supporting Information Figure S4) resulted in a significant increase in water interaction energy deviations (MUE of 1.8 kcal mol^{-1}). In the case of $[\mu\text{-(ferriheme)}_2O]^{4-}$, spin contamination precluded calculation of QM water interaction energies. Consequently, MM atomic charges were optimized based only on ESP data. Good qualitative agreement was obtained (Figure 1g,h). See Supporting Information Table S3 for a list of all atomic charges.

The MM model required the introduction of new atom types for Fe and axial ligands only (O_{ax} and H_{ax}). All structural parameters for the porphyrin ring system not involving new atom types were retained as described in CHARMM. On the other hand, new structural parameters were required to describe Fe−O_{ax} and Fe−N bonds, Fe−N−C_α, N−Fe−N, N−Fe−O_{ax}, Fe−O_{ax}−H_{ax}, and Fe−O_{oxo}−Fe angles, as well as the N*−Fe−C_α−C_α improper dihedral. Parameters for Fe−N and Fe−S from Autenrieth et al. were used as initial guesses for Fe−N and Fe−O_{H2O}, respectively (Table 2).[35] Initial guess values for all remaining new structural parameters were taken from ferrous heme in the CHARMM27 force field (Table 2). Parameters for ferrous Fe−O_2, Fe−$N_{histidine}$−C, N−Fe−N, Fe−N−C_α, and N*−Fe−C_α−C_α were used as initial guesses for ferric Fe−O_{HO} and Fe−O_{oxo}, Fe−O_{ax}−H_{ax}, N−Fe−N, Fe−N−C_α, and N*−Fe−C_α−C_α respectively. Where necessary, adjustments were made to these guess parameters to produce MM geometries which agreed with those calculated using DFT (OPBE/LANL2DZ) or (where available) average bond lengths and angles from crystal structures of related iron(III) porphyrins in the CSD. No changes were made to N−Fe−N and Fe−N−C_α guess parameters. Except for N−Fe−O_{ax} and Fe−O_{oxo}−Fe, changes were made to reference values (b_0 and θ_0) only (Table 2). In the case of the exceptions, alterations to force constants (K_θ) were required because six-coordinate heme models have an in-plane iron center. This is ensured by strong N*−Fe−C_α−C_α improper force constants and weak angle force constants. The iron center in the five-coordinate ferriheme species of interest in this study deviates from the porphyrin plane by up to 0.5 Å.[37] To accommodate this, the N*−Fe−C_α−C_α improper force constant was relaxed to the value used for C_α*−C_α−C_{meso}−N, necessitating larger K_θ values for N−Fe−O_{ax}. A larger K_θ was also required to maintain the near-linear Fe−O_{oxo}−Fe angle. Ideally force constants are altered to reproduce localized vibrations (obtained from QM calculation or vibrational spectroscopy), however, given complex vibrational coupling in the large ferriheme molecules, this is unfeasible. Instead, the smallest changes to these force constants were made that gave satisfactory structural agreement.

With the exception of $[H_2O\text{-ferriheme}]^-$, bond lengths and angles in the energy minimized MM models generally agreed with DFT values to within 0.03 Å and 3°, respectively (Table 3). While the Fe−N distance and N−Fe−O_{oxo} angle of $[\mu\text{-(ferriheme)}_2O]^{4-}$ fell just outside these ranges with respect to DFT, they agreed with experimental values. Fe−O_{ax} bond lengths for $[H_2O\text{-ferriheme}]^{0/-}$ species were somewhat longer than the average values of five-coordinate iron(III) porphyrin molecules in the CSD but still fell within the reported experimental range of 1.98−2.20 Å.[37] Despite complex coupling of vibrational modes of ferriheme mentioned above, a single prominent mode in $[\mu\text{-(ferriheme)}_2O]^{4-}$, the asymmetric Fe−$O_{oxo}$ bond stretch, was readily identified. The computed MM frequency of this mode agreed well with experiment (884 vs 880 cm^{-1}).[37]

MD Simulations. Eight ferriheme species were modeled in aqueous solution using the TIP4P-Ew water model. These included the three monomeric species $[HO\text{-ferriheme}]^{2-}$, $[H_2O\text{-ferriheme}]^-$, and $[H_2O\text{-ferriheme}]^0$; the dimeric $[\mu\text{-(ferriheme)}_2O]^{4-}$ species; and four π−π dimers $[(HO\text{-ferriheme})_2]^{4-}$, $[(HO\text{-ferriheme})(H_2O\text{-ferriheme})]^{3-}$, $[(H_2O\text{-ferriheme})_2]^{2-}$, and $[(H_2O\text{-ferriheme})_2]^0$. Production dynamics were recorded over 10 ns.

The porphyrin interplanar angles and distances, lateral shifts, and torsion angles between the ferriheme molecules for the π−π and μ-oxo dimers were analyzed. The π−π dimers remained associated over the entire course of the MD simulations and displayed little deviation from coplanarity. Of the 200 000 structures recorded for each ferriheme species, more than 80% had an interplanar angle less than 5° (Table 4 and Supporting Information Figure S5). The average interplanar distance was 3.4 ± 0.1 Å (Table 4) and agreed well with the average separation measured from crystal structures of π-stacked iron(III) porphyrin molecules (3.46 ±

Table 2. Initial Guess and Optimized Structural Parameters Used for Ferriheme Species[a]

	initial guess		optimized	
bonds	K_b (kcal mol^{-1} Å^{-2})	b_0 (Å)	K_b (kcal mol^{-1} Å^{-2})	b_0 (Å)
Fe–N	270.2	2.00[g]	270.2	2.18
Fe–O_{H2O}[b]	300.0	2.45[g]	300.0	2.25
Fe–O_{HO}[c]	250.0	1.80[h]	250.0	1.93
Fe–O_{oxo}[d]	250.0	1.80[h]	250.0	1.93
	initial guess		optimized	
angles	K_θ (kcal mol^{-1} rad^{-2})	θ_0 (deg)	K_θ (kcal mol^{-1} rad^{-2})	θ_0 (deg)
N–Fe–O_{H2O}[b]	139.30	103.90[h]	200.00	98.50
N–Fe–O_{HO}[c]	139.30	103.90[h]	155.00	107.00
N–Fe–O_{oxo}[d]	139.30	103.90[h]	139.30	103.00
Fe–O_{H2O}–H_{H2O}[b]	33.00	133.00[h]	33.00	130.00
Fe–O_{HO}–H_{HO}[c]	33.00	133.00[h]	33.00	128.00
Fe–O_{oxo}–Fe[d]	160.00	130.60[h]	200.00	180.00
	initial guess		optimized	
improper	K_ω (kcal mol^{-1} rad^{-2})	ω_0 (deg)	K_ω (kcal mol^{-1} rad^{-2})	ω_0 (deg)
N*–C_α–C_α–Fe	137.40	0.00[h]	18.30	0.00
	initial guess		optimized	
nonbonded	ε (kcal mol^{-1})	$R_{min}/2$ (Å)	ε (kcal mol^{-1})	$R_{min}/2$ (Å)
Fe[e]	−0.0200	1.4443	−0.0200	1.4443
$O_{H2O}/O_{HO}/O_{oxo}$[f]	−0.1521	1.7682	−0.1521	1.7682
$H_{H2O/HO}$[f]	−0.0460	0.2245	−0.0460	0.2245

[a] See eq 3 for description of force field parameters. [b] $[H_2O\text{-ferriheme}]^{0/-}$. [c] $[HO\text{-ferriheme}]^{2-}$. [d] $[\mu\text{-(ferriheme)}_2O]^{4-}$. [e] Fe^{3+} parameters taken from de Hatten et al. for Fe^{2+}.[47] Autenrieth et al. similarly used Fe^{2+} nonbonded parameters for Fe^{3+}. [f] From CHARMM27 for OT and HT atom types. [g] From Autenrieth et al.[35] [h] From CHARMM27.

Table 3. DFT (OPBE/LANL2DZ), MM-Minimized and Experimental Bond Lengths (Å), Angles (deg), and Iron out of Plane (OOP) Deviations (Å) for Ferriheme Species[a]

	Fe–O_{ax}	Fe–N	Fe–O_{ax}–X	N–Fe–O_{ax}	N–Fe–N	Fe–N–C_α	OOP[e]
$[HO\text{-ferriheme}]^{2-}$							
DFT	1.88	2.13(2)	119.9[b]	103.7(4)	86.8(6)	126.0(7)	0.5
CHARMM	1.88	2.097(3)	119.8[b]	103.1(3)	87.1(4)	126.9(3)	0.5
Exp.	*1.85(2)*	*2.07(1)*	–[c]	*102.6(8)*	*87.3(4)*	*126.3(2)*	*0.45(3)*
$[H_2O\text{-ferriheme}]^{-}$							
DFT	2.28	2.077(6)	110(4)[b]	95(5)	89.6(5)	128.8(3)	0.2
CHARMM	2.18	2.069(2)	120.3(3)[b]	98.3(4)	88.8(3)	126.6(3)	0.3
$[H_2O\text{-ferriheme}]^{0}$							
DFT	2.20	2.074(8)	121.6(2)[b]	96(2)	89.4(3)	126.6(3)	0.2
CHARMM	2.18	2.077(1)	121.1(2)[b]	98.2(2)	88.8(3)	126.8(2)	0.3
Exp.	*2.09(6)*	*2.00(4)*	–[c]	*93(3)*	*89.7(4)*	*126(1)*	*0.23(4)*[f]
$[\mu\text{-(ferriheme)}_2O]^{4-}$							
DFT	1.80	2.13(1)	177.8[d]	105(5)	86.1(4)	126(1)	0.6
CHARMM	1.78	2.085(2)	179.1[d]	99.4(8)	88.5(3)	125.6(7)	0.3
Exp.	*1.76(1)*	*2.08(2)*	*176(3)*[d]	*103(2)*	*87(1)*	*125(3)*	*0.48(4)*

[a] Experimental values are averages for all reported Fe(III) porphyrin crystal structures with the same axial ligands. [b] X = H. [c] Not available. [d] X = Fe. [e] Deviation from least-squares plane through nitrogen atoms. [f] Average of five-coordinate iron(III) porphyrins only.

0.07 Å).[56] Porphyrin lateral shifts were calculated using the center of mass of the porphine moiety. This is close to the position of the iron atom and thus approximates the lateral displacement between iron centers. All π-stacked dimers shared a similar profile with most lateral shifts close to 2 Å (see Table 4 and Supporting Information Figure S5). Finally, torsion angles between the porphyrin rings were measured using a dihedral defined by the meso carbon between propionate side chains and center of mass of the porphine. Dihedral values of 0° and 180° thus represent structures in which the propionate groups were eclipsed and anti to one another, respectively. Interestingly, the anti conformation was seldom observed. Rather, angles of ±60° and to a lesser extent ±120° were favored. Time series indicated lengthy periods in particular orientations which then suddenly switched to a new orientation (Supporting Information Figure S6).

The lateral shift for $[\mu\text{-(ferriheme)}_2O]^{4-}$ was smaller than that in the π–π dimeric species and had a narrower distribution owing to the constraining effect of the Fe–O_{oxo}–Fe bond (see Table 4 and Supporting Information Figure S7). On the other hand, the porphyrin interplanar angle was markedly greater where more than 75% of structures had an angle between 20 and 26° (see Table 4 and Supporting Information Figure S7). Unlike the π–π dimer, $[\mu\text{-(ferriheme)}_2O]^{4-}$ adopted an anti

Table 4. Average Interplanar Angles (deg), Distances, and Lateral Shifts (Å) of $\pi-\pi$ Dimeric Ferriheme and [μ-(ferriheme)$_2$O]$^{4-}$ Calculated from MD Simulations[a]

species	interplanar angle	interplanar distance	lateral shift
$[(HO\text{-ferriheme})_2]^{4-}$	3(4)	3.4(1)	1.8(7)
$[(HO\text{-ferriheme})(H_2O\text{-ferriheme})]^{3-}$	3(3)	3.4(1)	1.7(7)
$[(H_2O\text{-ferriheme})_2]^{2-}$	3(4)	3.4(1)	2.1(8)
$[(H_2O\text{-ferriheme})_2]^{0}$	3(4)	3.4(1)	1.7(6)
$[(H_2O\text{-ferriheme})_2]^{2-}$[b]	0[c]	3.7[c]	2.0−4.0[d]
$[\mu\text{-(ferriheme)}_2O]^{4-}$	24(11)	5.1(2)	1.1(2)

[a] Standard deviations of the least significant digit in parentheses. [b] From de Villiers et al. using an implicit water model and force field derived from that of Allinger.[29] [c] Fixed values. [d] Range containing 90% of structures.

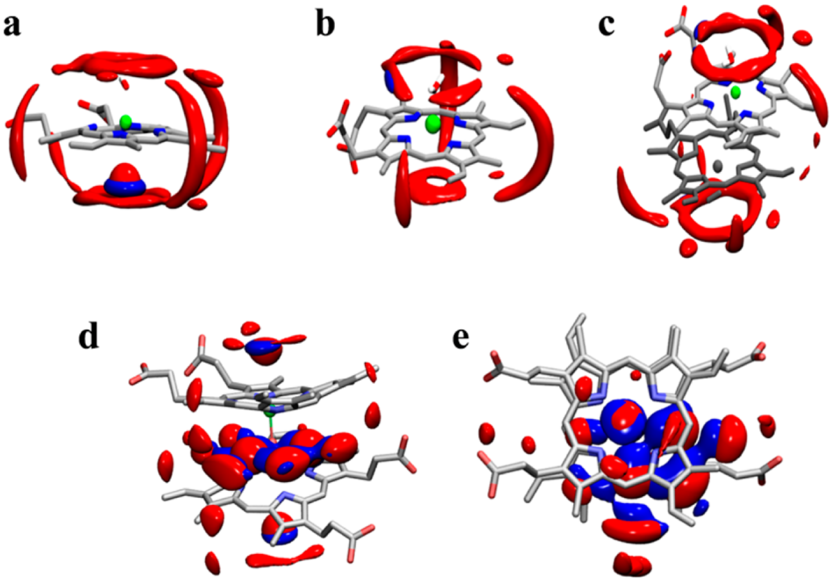

Figure 2. SDFs representing the distribution of water O (red) and H atoms (blue) solvating ferriheme species at 50% greater density than bulk. (a) $[HO\text{-ferriheme}]^{2-}$; (b) $[H_2O\text{-ferriheme}]^{-}$; and (c) $[(HO\text{-ferriheme})(H_2O\text{-ferriheme})]^{3-}$ and $[\mu\text{-(ferriheme)}_2O]^{4-}$ (d) side and (e) top views. Iron atoms are represented by green spheres, and the lower ferriheme molecule in (c) is colored gray to aid visualization. See Supporting Information Figures S8 and S9 for SDFs of all monomeric and $\pi-\pi$ dimer species.

conformation in which the dihedral angles fluctuated around 180°.

Aqueous solvation of ferriheme species was investigated using SDFs as previously described for other metal complexes.[48,53] Owing to the flexibility of the propionate side-chains, solvation of only the porphyrin ring is described. Monomeric ferriheme species displayed three main regions with high probabilities of hydration by water O atoms (see Figure 2 and Supporting Information Figure S8), similar to that reported for ferrous heme by Cuya Guizado and co-workers.[57] Highly solvated areas included the axial water and hydroxide ligands, H_{meso} on the porphyrin ring, and the unligated face. Strong solvation of the axial ligands is expected given the propensity of water and hydroxide molecules to hydrogen bond. The cage-like structure surrounding H_{meso} atoms resembles that observed in aromatic molecules such as benzene[58] but is less complete owing to the flexibility of the propionate side chains which limit water interaction with the H_{meso} atom between them. Interestingly, solvation of the unligated face presented in two forms. The first was observed for $[H_2O\text{-ferriheme}]^{0}$ and $[HO\text{-ferriheme}]^{2-}$, where a single water molecule was situated close to the sixth coordination site of the iron center. The point of highest probability in this region for these species occurred at 3.1 and 3.0 Å, respectively. The second type of solvation of the unligated face was observed for $[H_2O\text{-ferriheme}]^{-}$. Here, hydrogen atoms of water molecules oriented toward the negative potential of the pyrrole nitrogen atoms. Since the QM ESPs of $[H_2O\text{-ferriheme}]^{-}$ and $[HO\text{-ferriheme}]^{2-}$ showed similar negative potential radiating from the unligated face (see Figure 1), solvation of these two molecules was expected to be similar. Given the difficulty in reproducing the ESP of the unligated face of $[HO\text{-ferriheme}]^{2-}$ (see above), the solvation shown in Figure 2a is probably less convincing than the rest.

Solvation of $\pi-\pi$ dimeric species was similar to that observed for monomeric species with the obvious exception of the unligated face (see Figure 2c and Supporting Information Figure S9). While solvation still predominated around the axial ligands, the cage-like structures around H_{meso} atoms were less defined. The SDF of $[\mu\text{-(ferriheme)}_2O]^{4-}$ was markedly different from those of the monomeric and $\pi-\pi$ dimeric species (see Figure 2d,e). Strong solvation of the axial oxide bridge by two water molecules was observed throughout the trajectory, while a third was present at slightly lower probability. It is this solvation of the axial bridging ligand which causes the greater porphyrin interplanar angle (see above). Loss and return of the third water molecule could be clearly seen throughout the course of the simulation where its absence produced a decrease in Fe−Fe distance and a corresponding increase in interplanar angle (see Figure 3). A second solvation shell around the two strongly solvating water molecules and hydration of the unligated face by a single water O atom was also observed.

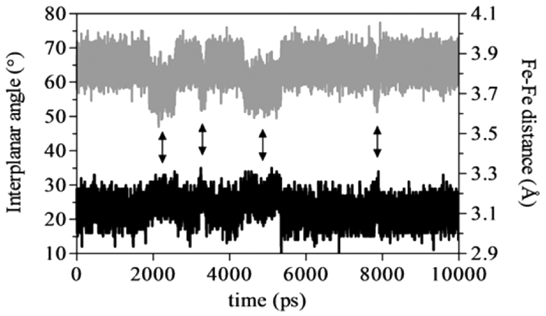

Figure 3. Fe−Fe distance (gray, right axis) and porphyrin interplanar angle (black, left axis) of $[\mu\text{-(ferriheme)}_2O]^{4-}$ over the course of MD simulation. Arrows indicate effects on structure when only two water molecules interacted with the oxide bridge.

EXAFS. EXAFS has previously been used to probe hemin in the solid state,[59−61] as well as to investigate solid state aggregates of hemin,[60,61] hemozoin,[62] β-hematin (synthetic hemozoin), and its analogues in both solid and solution state.[63−66] To obtain experimental evidence for ferriheme structures in solution, EXAFS was employed in this work. Experimental conditions necessitated concentrations above 1 mM ferriheme, thus precluding measurement of monomeric species. Furthermore, the cryoprotectant PEG400 used to prevent glassing at the low temperature required to limit thermal motion was found to induce μ-oxo dimer formation. This was confirmed using magnetic susceptibility measurements under conditions similar to those employed by Asher et al.[30] for water miscible organic solvents (40% (v/v) alkaline aq. PEG400) where a magnetic moment of 2.40 μ_B was obtained, close to the value expected for μ-oxo dimeric ferriheme (2.0 ± 0.1 μ_B).[33] Under conditions used for investigation of π−π dimers (aq. solution, pH 7.4), addition of the required 20% (v/v) PEG400 induced approximately 20% μ-oxo dimer (magnetic moment of 4.2 μ_B). Thus, measurements could only be confidently conducted on the μ-oxo dimer induced with 40% (v/v) alkaline aq. DMSO with 20% (v/v) PEG400 (it should be noted that this solution is still about 84% H_2O by mol).

The EXAFS spectrum of the frozen solution of $[\mu\text{-(ferriheme)}_2O]^{4-}$ was markedly different from that of the dried solid sodium salt previously prepared via precipitation from aqueous acetone (Figure 4a,b).[37] The spectrum of the solid was well fitted using the reported crystal structure of μ-oxo ferriheme dimethyl ester as an input model for the fit (Figure 4c,d).[42] On the other hand, this structure produced a poor fit when used as an input model for the frozen solution spectrum. Consequently, an alternative model was needed. For this purpose structures from the MD simulation were used. Three structures were considered, that furthest from the average calculated over the course of the MD simulation, one in which the porphyrin core structure only was furthest from its average, and that closest to the average (see Supporting Information Tables S4 and S5). Owing to the relatively low conformational freedom of the system, all three gave essentially the same result. Further discussion is confined to the last case. The EXAFS spectrum of the frozen solution was poorly fitted using the average solution structure of $[\mu\text{-(ferriheme)}_2O]^{4-}$ from MD simulation unless solvation was taken into account (Figure 4e,f). On the other hand, when four water molecules surrounding the oxide bridge and one on the unligated face were included at positions obtained from the SDF, an excellent fit was achieved (Figure 4g,h). Incorporation of fewer water molecules in the model gave poorer fits. A comparison of interatomic distances obtained from fitting of EXAFS spectra shown in parts c, d and g, h of Figure 4 with those in the crystal structure of μ-oxo ferriheme dimethyl ester and the average distances from MD simulation are listed in Table 5.

The structure closest to the average in the MD simulation was used as input geometry to fit the EXAFS spectrum of the frozen solution (Figure 4g,h). Two water O atoms (one with $N = 4$ and the other with $N = 1$) placed at positions of highest probability density in the SDF near O_{oxo} and the unligated face of $[\mu\text{-(ferriheme)}_2O]^{4-}$, respectively, were included in the input structure. Fitting of EXAFS spectra was approached in a similar manner to that of Provost et al. and Karolewski et al. where the first- and second-order cumulants, ΔR and σ^2 respectively, were determined from MD simulation (see Experimental Section for details).[44,45] Calculated ΔR and σ^2 were adjusted using variable scaling factors, α and β, respectively, and optimized as part of the fitting process. These scale factors, as suggested by Karolewski et al.,[44] accounted for inaccuracies in experimental measurement, inherent errors in the predicted cumulants, and systematic differences between MD and EXAFS cumulants. Where possible, the same scaling factors were applied regardless of path. Five α-scaling factors were required to fit the experimental spectrum. Two separate values were required to describe water molecules on the unligated face and around O_{oxo}, termed $\alpha(1)_{wat}$ and $\alpha(2)_{wat}$, respectively. Two further values, α_{oxo} and α_{Fe}, described O_{oxo} and Fe of the adjacent porphyrin, while a third, α, described all other atoms. Only two β-scaling factors, β_{oxo} and β, were required to describe O_{oxo} and all the rest, respectively. Refinement statistics and optimized parameters from these fits are listed in Tables 6 and 7, respectively. Appropriate parameters for the solid and frozen solution fitted using a model that did not include waters of solvation are also given in Tables 6 and 7 for comparison.

Ideally, α and β scaling factors should be 0 and 1, respectively. However, since the EXAFS spectrum was recorded at lower temperature than that simulated (15 K vs 298 K), β scale factors which describe vibrational amplitudes are expected to be less than 1 in this case. On the other hand, changes in bond distances are not as markedly affected by differences in temperature, and thus α scale factors are expected to remain close to 0. In the case of the spectrum obtained from frozen solution fitted with included solvent molecules, α scaling factors were indeed close to ideal values. The β scaling factor that described all atoms other than O_{oxo} was slightly larger than expected, although its statistical significance spans 1. A larger value was obtained for β_{oxo}. This may stem from disorder around O_{oxo} arising from strong interactions with solvent molecules. Alternatively, force constants involving O_{oxo} may have been too strong in the MM model, not allowing sufficient motion around this ligand. Given the close agreement between the computed and experimental Fe−O_{oxo} asymmetric stretching frequency, the Fe−O_{oxo} force constant is probably not the cause of the discrepancy. The value of the force constant describing the Fe−O_{oxo}−Fe angle may be too large; however, this value was set at the minimum that gave acceptable geometric agreement and so within the limitations of the model this probably represents an optimum.

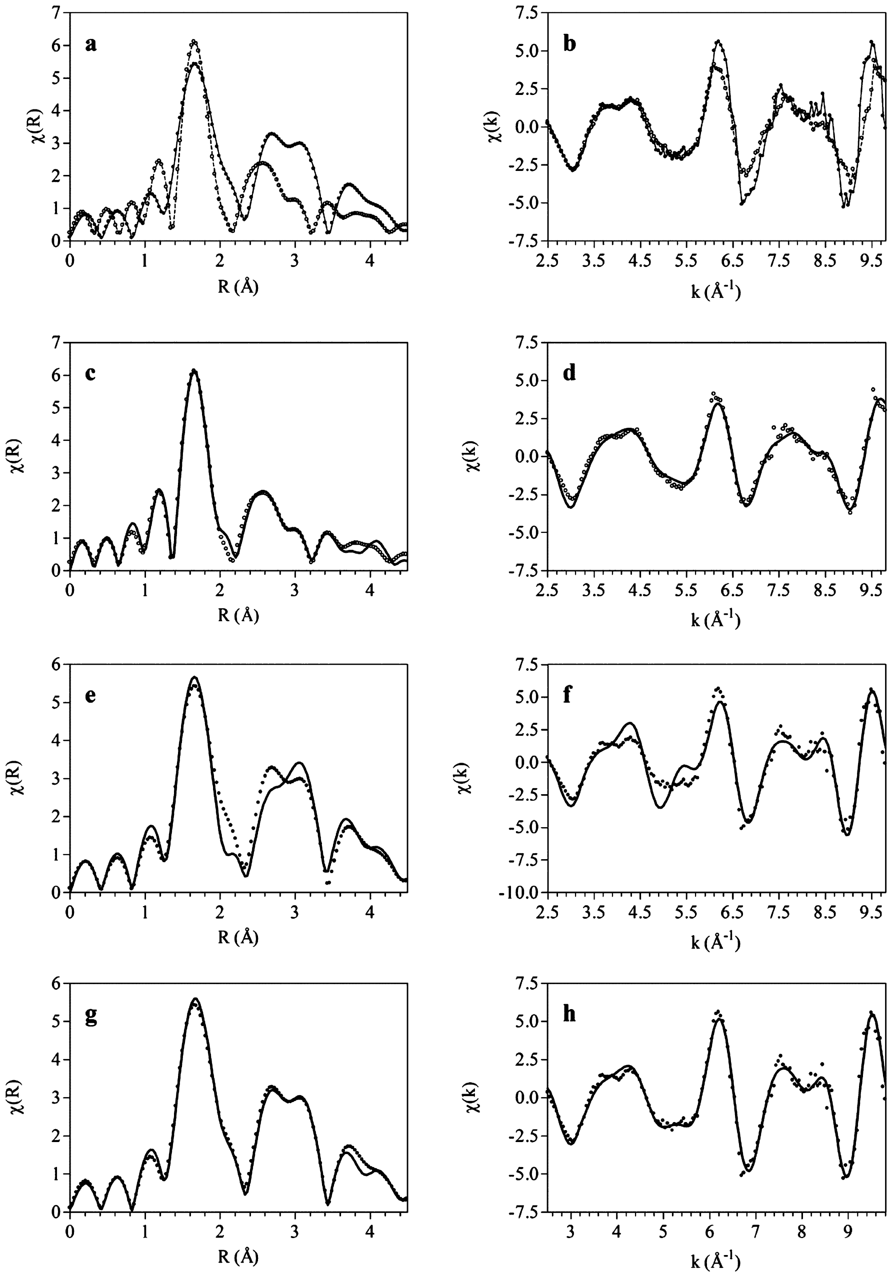

Figure 4. Experimental and fitted EXAFS spectra of $[\mu\text{-(ferriheme)}_2O]^{4-}$ in *R*- (left) and *k*-space (right). (a, b) Comparison of spectra recorded on frozen aqueous solution in 20% (v/v) aq. PEG400, 40% (v/v) DMSO, pH 10 at 15 K (closed circles) and dried solid precipitated as a sodium salt from aqueous acetone (open circles) recorded at 298 K. (c, d) Spectrum of the solid sample (open circles) fitted using the crystal structure of μ-oxo ferriheme dimethyl ester as input model (solid line).[42] (e, f) Spectrum of frozen solution (closed circles) fitted using the structure corresponding most closely to the average from MD simulation as input model (solid line), but not taking into account solvent molecules. (g, h) Spectrum of frozen solution (closed circles) fitted using the structure corresponding to the average from MD simulation but including solvent water molecules positioned with the aid of the SDF as input model (solid line). In (c and d), spectra were fitted over the range $1 \leq R \leq 4.4$ Å and $2.3 \leq k \leq 12.0$ Å^{-1} in *R*- and *k*-space, respectively, with k^3-weighting. In (e–h), spectra were fitted over the range $1 \leq R \leq 4.3$ Å and $2.4 \leq k \leq 9.8$ Å^{-1} in *R*- and *k*-space, respectively, with k^3-weighting.

■ DISCUSSION

The focus of this study was to probe structures of ferriheme species in aqueous solution using MD simulations. Force field parameters for nonprotein bound ferriheme models were thus developed for this purpose. Since ferriheme dimerizes under aqueous conditions,[29,30] discussion is concentrated on $\pi-\pi$ and μ-oxo dimers. In the case of the latter, it was feasible to collect EXAFS data which could be used to support the computational findings.

Solution Structure of $[\mu\text{-(ferriheme)}_2O]^{4-}$. Major solvation of the μ-oxo dimer (indicated by the SDF) occurred around the oxide bridge, a region displaying substantial negative potential in the ESP (Figure 1g,h). As a further test of this unexpected result, the ESP of the neutral μ-oxo ferriporphine analogue was calculated both in vacuum and using an implicit water model (SMD) employing the OPBE functional with three different basis sets (LANL2DZ, 6-31G*, and LANL2TZ*) and a different functional (B3LYP) with 6-31G*. All confirmed the negative potential around the oxo

Table 5. Comparison of Fitted EXAFS Interatomic Distances and Those Obtained from the Reported Crystal Structure of μ-oxo Ferriheme Dimethyl Ester[42] and from MD Simulation of $[\mu\text{-(ferriheme)}_2\text{O}]^{4-}$ in Aqueous Solution[a]

	solid		frozen solution	
distance	EXAFS[e]	crystal structure[f]	EXAFS[g]	MD[h]
$\text{Fe}-\text{O}_{\text{oxo}}$	1.793(8)	1.748(3)	1.87(1)	1.92(4)
Fe−N[b]	2.06(1)	2.08(1)	2.080(5)	2.11(3)
$\text{Fe}-\text{C}_\alpha$[b]	3.05(2)	3.08(2)	3.072(7)	3.12(4)
$\text{Fe}-\text{C}_\beta$[b]	4.40(2)	4.30(2)	4.31(1)	4.37(5)
$\text{Fe}-\text{C}_{\text{meso}}$[b]	3.44(5)	3.42(2)	3.388(8)	3.45(5)
Fe−Fe	3.5(2)	3.48	3.56(4)	3.83(7)
$\text{Fe}-\text{O(1)}_{\text{wat}}$[c]	–[j]	–[j]	2.48(1)	3.01[i]
$\text{Fe}-\text{O(2)}_{\text{wat}}$[d]	–[j]	–[j]	3.48(1)	3.25[i]

[a] Values are averages with standard deviations of the least significant digit in parentheses for distances between Fe and all atoms of the type indicated. [b] Average value for degenerate atoms. [c] One water molecule positioned on the unligated face of a given ferriheme molecule. [d] Four water molecules surrounding the bridging oxide ligand. [e] Dried precipitate obtained as a sodium salt from aqueous acetone solution and recorded at 298 K. [f] μ-oxo ferriheme dimethyl ester.[42] [g] Frozen aqueous solution in 20% (v/v) aq. PEG400, 40% (v/v) DMSO, pH 10 recorded at 15 K. [h] Average from 10 ns MD simulation in TIP4P-Ew water box. [i] Initial water positions identified from the points of highest probability in the SDF. [j] Not applicable.

Table 6. Refinement Statistics Determined from EXAFS Fitting of the Frozen Solution and Solid-State Spectra of the Sodium Salt of $[\mu\text{-(ferriheme)}_2\text{O}]^{4-}$ Recorded at 15 and 298 K, Respectively

statistics	solution[d]	solution[e]	solid[f]
R[a]	0.069	0.005	0.009
χ^2[a]	11.3	1.3	1.11
ε_k	0.0015	0.0015	0.0012
N_{ind}[b]	21.2	21.4	20.73
$N_{\text{var.}}$[c]	7	12	14

[a] Values of R and χ^2 were calculated in R-space.[39,41] [b] Number of independent data points.[39,41] [c] Number of variables used in the fit. [d] Spectrum recorded at 15 K fitted using the MD data without solvent water molecules as input model. [e] Spectrum recorded at 15 K fitted using the MD data including five water molecules at positions identified from the SDF as input model. [f] Spectrum recorded at 298 K fitted using the crystal structure of μ-oxo ferriheme dimethyl ester as input model.[42]

bridge (see Supporting Information Figure S10). Furthermore, similarly positioned solvent molecules (benzene, acetonitrile, toluene, methyl acetate, or water) have been reported in crystal structures of μ-oxo dimers of synthetic Fe(III) porphyrins. In all of these, an H atom is oriented toward the oxo bridge.[67−71] In addition, water molecules were found close to the sixth coordination site which also possesses marked negative potential. This solvated model of $[\mu\text{-(ferriheme)}_2\text{O}]^{4-}$ could be successfully fitted to the observed EXAFS spectrum in frozen aqueous DMSO solution only if water molecules were included in the refinement (Figure 4 part g versus part e and part h versus part f). Notably, the observed EXAFS spectrum of dried solid $\text{Na}_4[\mu\text{-(ferriheme)}_2\text{O}]$ differed markedly from that of the frozen solution (Figure 4a,b) and could be well fitted using the crystal structure of μ-oxo ferriheme dimethyl ester[42] which contains no solvent molecules (Figure 4c,d). With the exception of the Fe−Fe distance, interatomic distances from the Fe center observed in the fitted EXAFS spectrum from frozen solution were very close to those in the MD simulation (Figure 5a, atomic coordinates in Supporting Information Table S6), falling within two standard deviations from the average distances in the MD simulation. Although the fitted Fe−Fe distance of 3.56 ± 0.04 Å was significantly shorter than the average from MD simulation (3.83 ± 0.07 Å), structures with this distance were indeed observed in the simulation with little effect on other distances. The difference could have arisen from the different solvent composition and temperature favoring a small change in conformation in the frozen solution, or it may arise from too strong an Fe−O−Fe bending force constant in the MM force field. On the other hand, it should be noted that an observed EXAFS spectrum in solution is in fact an average of the spectra of all conformations present and not the spectrum of the average structure. Thus, a perfect match with the average structure would not generally be expected. Nonetheless, the small deviations of the average simulated distances from the fitted EXAFS distances indicate that variation of the scattering potentials due to thermal vibrations or slight structural disorder is apparently quite small. This is consistent with the fact that similar fitted structures were obtained when using initial structures from frames furthest from the average in the MD simulation as mentioned above.

Five solvent molecules were required to fit the EXAFS spectrum, corresponding to four degenerate O atoms around the oxide bridge and one O atom on the unligated face. Initial positions were based on points of highest probability in the SDF. In the case of water molecules around the μ-oxo bridge, final fitted distances ($\text{Fe}-\text{O(2)}_{\text{wat}}$) were slightly longer than initial values, but all fell well within the 50% greater than bulk isosurfaces of the SDF (Figure 5b). The points of highest probability in the SDF do not necessarily correspond to the average points. The small difference in final positions may simply be a reflection of this. Differences in solvent composition may also affect solvation. In the case of the unligated face, the $\text{Fe}-\text{O(1)}_{\text{wat}}$ distance in the fitted structure (2.48 ± 0.01 Å) fell partway between that expected for outer sphere solvation (3.3 Å) and that of coordinated H_2O (2.1 Å), suggesting that an equilibrium may exist between 5- and 6-coordinate Fe(III). The fitted distance is too short to be consistent with a noncovalent interaction (e.g., purely outer sphere solvation or π-stacking), but too long for a coordination bond. Furthermore, a search of the CSD for Fe(III) porphyrins with axial O ligands found 49 six-coordinate and 197 five-coordinate complexes, indicating a relatively small energy difference between these two configurations. The equilibrium proposed thus seems quite plausible.

An interesting structural feature observed in the MD simulation is that the porphyrin interplanar angle was quite large (averaging about 23°). This arose from the entry of water between the porphyrin rings with formation of a hydrogen bond to the μ-oxo bridge. This interplanar angle does not resemble that found in crystal structures of μ-oxo Fe(III) octaethylporphyrin and μ-oxo ferriheme dimethyl ester, where the corresponding angles are 2 and 7°, respectively.[42,72] While it is closer to that observed in the μ-hydroxo dimer of Fe(III) octaethylporphyrin (about 30°),[73] the average $\text{Fe}-\text{O}_{\text{oxo}}-\text{Fe}$ angle (168°) was closer to that of μ-oxo Fe(III) octaethylporphyrin (179°) and μ-oxo ferriheme dimethyl ester (170°)[42,72] and not that of the μ-hydroxo dimer of Fe(III) octaethylporphyrin (142°).[73] The large interplanar angle arises from distortion of the porphyrin planes. Indeed, formation of a μ-

Table 7. Refined Parameters for Fitted EXAFS Spectra of $[\mu\text{-(ferriheme)}_2O]^{4-}$ in Frozen Solution and the Solid State Recorded at 15 and 298 K, Respectively[a,b]

	solution[c]	solution[d]	solid[e]
S_0^2	0.80(1)	0.80(3)	1.0(1)
ΔE_0	2(1)	0.1(6)	−0.9(9)
α	−0.004(4)	−0.012(2)	–[f]
α_{oxo}	0.05(1)	0.029(7)	–[f]
α_{Fe}	−0.02(5)	−0.05(1)	–[f]
$\alpha(1)_{wat}$	–[f]	−0.174(3)	–[f]
$\alpha(2)_{wat}$	–[f]	0.072(4)	–[f]
β	0.7(6)	1.3(4)	–[f]
β_{oxo}	2(2)	2.5(8)	–[f]

First- and Second-Order Cumulants

	initial[h]		solution[c]		solution[d]		solid[e]	
	N[g]	σ^2	ΔR	σ^2	ΔR	σ^2	ΔR	σ^2
Fe−O_{oxo}	1	0.0016	0.09(2)	0.003(2)	0.06(1)	0.004(1)	0.044(8)	0.0023(6)
Fe−N	4	0.0010	−0.009(8)	0.0007(6)	−0.025(5)	0.0013(3)	−0.021(5)	0.0037(9)
Fe−C_α	8	0.0017	−0.01(1)	0.001(1)	−0.037(7)	0.0023(6)	−0.026(8)	0.005(1)
Fe−C_β	8	0.0023	−0.02(2)	0.002(1)	−0.05(1)	0.0031(8)	0.10(2)	0.004(4)
Fe−C_{meso}	4	0.0025	−0.01(1)	0.002(2)	−0.041(8)	0.0033(9)	0.03(4)	0.004(4)
Fe−Fe	1	0.0044	−0.1(2)	0.003(3)	−0.18(4)	0.006(2)	0.0(2)	0.01(2)
Fe−$O(1)_{wat}$	1	0.0020	–[f]	–[f]	−0.52(1)	0.0008(9)	–[f]	–[f]
Fe−$O(2)_{wat}$	4	0.0020	–[f]	–[f]	0.23(1)	0.001(1)	–[f]	–[f]

[a] Standard deviation of the least significant digit given in parentheses. [b] See text for explanation of parameters. [c] Spectrum recorded at 15 K fitted using the MD data without solvent water molecules as input model. [d] Spectrum recorded at 15 K fitted using the MD data including five water molecules at positions identified from the SDF as input model. [e] Spectrum of the sodium salt recorded at 298 K fitted using the crystal structure of μ-oxo ferriheme dimethyl ester as input model.[42] [f] Not applicable. [g] Degeneracy. [h] Initial values determined from MD simulation using eq 2 and a β value of 1.

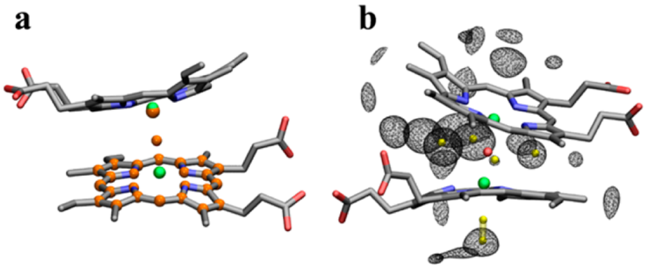

Figure 5. Structure of aqueous $[\mu\text{-(ferriheme)}_2O]^{4-}$ determined by MD simulation compared to the positions of atoms fitted to reproduce the observed EXAFS spectrum. Fitted porphyrin atoms and O^{2-} bridging ligand in (a) are shown in orange and solvent water O atoms in (b) in yellow. Wireframe isosurfaces in (b) represent the SDF of water O atoms at 50% greater density than bulk. All O atoms around the μ-oxo bridge fall inside the SDF isosurfaces. The O atom on the unligated face was fitted at a distance of 2.48 Å from Fe (green spheres) and may correspond to an equilibrium between outer sphere solvation and coordinated water. This is indicated by two positions on the lower face. For the sake of clarity, fitted porphyrin and solvent O atoms are shown separately in (a) and (b). The figure shows scattering atoms fitted for the lower Fe(III) ion only.

hydroxo dimer of ferriheme is not supported by experiment since strong antiferromagnetic coupling is observed,[37] incompatible with a μ-hydroxo species.[74−76]

Monomeric and π−π Dimeric Ferriheme in Solution. The dominant forms of ferriheme in purely aqueous media are π−π dimers.[29−31] Results of MD simulations were consistent with this. With no constraints imposed to maintain the intermolecular interactions between porphyrins, these dimers remained associated throughout the simulation regardless of their charge. Furthermore, despite the ESPs indicating that the propionate groups possess the greatest negative potential in these molecules (Figure 1), they showed no propensity to interact with the Fe(III) center of the neighboring porphyrin. This is consistent with a previous study in which it was shown that these groups preferentially interact with solvent water molecules.[77] Indeed, water interaction energy calculations in Table 1 demonstrate this strong interaction. This finding agrees with the observation that β-hematin does not form spontaneously in purely aqueous solution without a mediator or interface.[77] The stability of $[(H_2O\text{-ferriheme})_2]^0$ has been questioned by Crespo et al.[31] who have suggested that electrostatic repulsion between the formal net positive charges around the Fe(III) centers of the porphine cores of this species would cause dissociation to monomers. In the simulation this was found not to be the case. While it is true that the formal charge of the core of $[H_2O\text{-ferriheme}]^0$ is indeed cationic, in the present study summation of Mulliken atomic charges determined from DFT gave a value close to +0.5 rather than +1. Mulliken atomic charges of the propionate group summed to a value of approximately −0.3 rather than −1, while the charge on the propionic acid side chain remained close to 0. Thus, charge is in fact delocalized over the porphyrin ring and so the proposal by Crespo et al. of a strongly cationic porphine core leading to dissociation in the neutral species was not supported.

Lateral shifts and porphyrin orientations of π−π dimeric ferriheme have previously been investigated using MD in an implicit water model with the HYPERCHEM software package and a force field derived from that of de Allinger (see Table 4).[29] With the porphyrin rings constrained to be coplanar, the lateral shift lay between 2.5 and 3.0 Å and the preferred torsion angles of porphyrin rings were ±135 or 180°. In our study using an explicit water model without constraints between porphyrin rings, lateral shifts were found to be closer to 2.0 Å (see Table 4) and little deviation from coplanarity was observed. Most porphyrin structures had torsion angles of ±60°, despite starting structures having propionate groups positioned at 180° (see Supporting Information Figure S6). By contrast with the μ-oxo dimer, these angles did not remain fixed over the course of the simulation. In vacuum, torsion angles of 180° are expected since the electrostatic repulsion between negatively charged propionate groups is then minimized. In solution, however, solvation by water molecules screens electrostatic repulsion and facilitates the closer orientation of propionate groups.

SDFs of ferriheme monomers indicated that there is prominent solvation of the unligated face. In the case of $[\text{HO-ferriheme}]^{2-}$ and $[\text{H}_2\text{O-ferriheme}]^{0}$ species, the position of the solvent water molecule is analogous to that seen for the unligated face of $[\mu\text{-(ferriheme)}_2\text{O}]^{4-}$. Interestingly, the porphyrin macrocycle is generally regarded as hydrophobic, playing a key role in the binding of heme to proteins.[78] Strong hydration of the unligated face indicated by the SDFs suggests that these surfaces may be less hydrophobic than previously believed.

Effect of Solvent on Ferriheme Speciation. Previous studies have shown that solvation plays a crucial role in determining ferriheme speciation.[21,30] Aqueous mixtures of protic water-miscible solvents have been shown to favor $\pi-\pi$ dimer formation, while mixtures of aprotic solvents induce the μ-oxo dimer at high pH. Furthermore, formation of the μ-oxo dimer was associated with an increase in entropy.[30] These observations were rationalized by Asher et al. on the basis of solvation and desolvation of the porphyrin. At high pH the ferriheme axial ligand is hydroxide. Protic solvents that can act as both hydrogen bond donors and acceptors can replace solvating water molecules around this ligand, while aprotic solvents have a reduced capacity to replace these water molecules because they are hydrogen bond acceptors only. The result is that an increased concentration of water molecules compared to the bulk will be necessary to satisfy the hydrogen bonding requirements of the hydroxide ligand. This would decrease the entropy of the system and was proposed to drive formation of the μ-oxo dimer, presumably through the loss of a water ligand, two hydrogen ions, and the solvation shell associated with the axial ligands when this species is formed.[30] In our study the SDFs of monomeric and $\pi-\pi$ dimeric ferriheme clearly showed prominent solvation of axial ligands by O atoms of water (Figure 2). Although visually obscured, there was also significant solvation by H atoms of water, consistent with its role as a hydrogen bond donor to the axial ligands. The SDF calculated for $[\mu\text{-(ferriheme)}_2\text{O}]^{4-}$ showed strong solvation of the μ-oxo bridging ligand. In agreement with the previous hypothesis, the fact that the oxide ion is shared between the two porphyrins ought to result in a drastic reduction in the degree of solvation of the ligated faces.

■ CONCLUSIONS

MD simulations using CHARMM in combination with EXAFS data has proven to be a useful approach to elucidate the solution structure of $[\mu\text{-(ferriheme)}_2\text{O}]^{4-}$. The μ-oxo bridge was found to be strongly solvated, while the outer face of the porphyrins were solvated at the axial position, suggesting possible equilibrium binding of water to the sixth coordination site. Simulations also strongly supported the proposed predominance of $\pi-\pi$ dimers in aqueous solution, which exhibit coplanar interactions between the unligated faces of five-coordinate ferriheme species. These appeared to be stable in both neutral and anionic forms. MD calculation confirmed previous suggestions that the faces of monomeric and $\pi-\pi$ dimeric species bearing the axial ligands are strongly solvated. The unligated faces of monomeric species were also considerably solvated.

The results from this study suggest that the model developed in this work is likely to be useful for investigating other ferriheme complexes. It is now being used to probe the interaction between ferriheme and antimalarial drugs.

■ ASSOCIATED CONTENT

Ⓢ Supporting Information

Values of R_i and $\langle (R_{i,\text{ave}} - R_i)^2 \rangle$ calculated from MD simulation of $[\mu\text{-(ferriheme)}_2\text{O}]^{4-}$ used in EXAFS refinement; CHARMM topology and atom-typing of ferriheme models; selected structural properties of $[\text{HO-ferriheme}]^{2-}$ calculated using DFT (OPBE/LANL2DZ) in $S = {}^5/_2$ and ${}^3/_2$ spin states; water interaction energy labeling scheme; ESP of $[\text{HO-ferriheme}]^{2-}$ generated using MM atomic charges which produce good agreement with QM ESP; optimized atomic charges of ferriheme species; interplanar angles, lateral shift, and porphyrin torsion histograms of $\pi-\pi$ dimers; lateral shift, interplanar angle, and torsion angle histograms of $[\mu\text{-(ferriheme)}_2\text{O}]^{4-}$; SDFs of monomeric and $\pi-\pi$ dimeric ferriheme; EXAFS interatomic fitted distances and refinement parameters for $[\mu\text{-(ferriheme)}_2\text{O}]^{4-}$; QM ESPs of μ-oxo ferriporphine calculated in vacuum and implicit solvent; atomic coordinates for fitted EXAFS model. This material is available free of charge via the Internet at http://pubs.acs.org.

■ AUTHOR INFORMATION

Corresponding Authors

*(K.J.N.) Tel.: +27-21-650-2542. Fax: +27-21-650-5195. E-mail: kevin.naidoo@uct.ac.za.
*(T.J.E.) Tel.: +27-21-650-2528. Fax: +27-21-650-5195. E-mail: timothy.egan@uct.ac.za.

Notes

The authors declare no competing financial interest.

■ ACKNOWLEDGMENTS

Financial support for this work was provided by the National Research Foundation (NRF). Any opinion findings and conclusions or recommendations expressed in this material are those of the author(s) and therefore the NRF do not accept any liability in regard thereto. The University of Cape Town is also acknowledged for financial support. Part of this work was based upon research supported by the South African Research Chairs Initiative (SARChI) of the Department of Science and Technology and the NRF awarded to K.J.N. We thank the Centre for High Performance Computing (CHPC) for use of their resources and acknowledge the use of the XAS beamline at the Australian Synchrotron, Victoria, Australia.

■ ABBREVIATION LIST:

CHES, *N*-cyclohexyl-2-aminoethanesulfonic acid; CSD, Cambridge Structural Database; DFT, density functional theory; ESPs, electrostatic surface potentials; EXAFS, extended X-ray absorption fine structure; Ferriheme, iron(III) protoporphyrin IX; LSP, least-squares plane; MD, molecular dynamics; MM, molecular mechanics; MS, multiple scattering; MUEs, mean unsigned errors; NPT, isobaric−isothermal ensemble; NVT, canonical ensemble; OOP, out of plane; PEG400, polyethylene glycol 400; QM, quantum mechanics; SDFs, spatial distribution functions

■ REFERENCES

(1) Tsiftsoglou, A.; Tsamadou, A.; Papadopolou, L. *Pharmac. Ther.* **2006**, *111*, 327−345.

(2) Chen, J.-J.; London, I. M. *Cell* **1981**, *26*, 117−122.

(3) Ishii, N. D.; Maniatis, G. M. *Nature* **1978**, *274*, 372−374.

(4) Tsiftsoglou, A.; Robinson, S. H. *Int. J. Cell Cloning* **1985**, *3*, 349−366.

(5) Monette, F. C.; Holden, S. A.; Sheehy, M. J.; Matzinger, E. A. *Exp. Hematol.* **1984**, *12*, 782−787.

(6) Tsiftsoglou, A.; Pappas, I. S.; Vizirianakis, I. S. *Pharmacol. Ther.* **2003**, *100*, 257−290.

(7) Mense, S. M.; Zhang, L. *Cell Res.* **2006**, *16*, 681−692.

(8) Suliman, H. B.; Carraway, M. S.; Velsor, L. W.; Day, B. J.; Ghio, A. J.; Piantadosi, C. A. *Free Radicals Biol. Med.* **2002**, *32*, 246−256.

(9) Schaer, D. J.; Buehler, P. W.; Alayash, A. I.; Belcher, J. D.; Vercellotti, G. M. *Blood* **2013**, *121*, 1276−1284.

(10) Kumar, S.; Bandyopadhyay, U. *Toxicol. Lett.* **2005**, *157*, 175−188.

(11) Schmitt, T. H.; Frezzatti, W. A.; Schreier, S. *Arch. Biochem. Biophys.* **1993**, *307*, 96−103.

(12) Robinson, S. R.; Dang, T. N.; Dringen, R.; Bishop, G. M. *Redox Rep.* **2009**, *14*, 228−235.

(13) Cassim, A. A.; DeBaun, M. R. *Annu. Rev. Med.* **2013**, *64*, 456−466.

(14) Krugliak, M.; Zhang, F.; Ginsburg, H. *Mol. Biochem. Parasitol.* **2002**, *119*, 249−256.

(15) Jeney, V.; Balla, J.; Yachie, A.; Varga, Z.; Vercellotti, G. M.; Eaton, J. W.; Balla, G. *Blood* **2002**, *100*, 879−887.

(16) Larsson, S. C.; Adami, H.-O.; Giovannucci, E.; Wolk, A. *J. Natl. Cancer Inst.* **2005**, *97*, 232−233.

(17) Pierre, F.; Tache, S.; Petit, C. R.; Van der Meer, R.; Corpet, D. E. *Carcinogenesis* **2003**, *24*, 1683−1690.

(18) Atamna, H.; Frey, W. H., II. *Proc. Natl. Acad. Sci. U.S.A.* **2004**, *101*, 11153−11158.

(19) Pramanik, D.; Dey, S. G. *J. Am. Chem. Soc.* **2011**, *133*, 81−87.

(20) Brown, S. B.; Dean, T. C.; Jones, P. *Biochem. J.* **1970**, *117*, 733−739.

(21) O' Keeffe, D. H.; Barlow, C. H.; Smythe, G. A.; Fuchsman, W. H.; Moss, T. H.; Lilienthal, H. R.; Caughey, W. S. *Bioinorg. Chem.* **1975**, *5*, 125−147.

(22) Graf, W.; Pommerening, K.; Scheler, W. *Acta Biol. Med. Ger.* **1971**, *26*, 895−909.

(23) Moreau, S.; Perly, B.; Biguet, J. *Biochimie* **1982**, *64*, 1015−1025.

(24) Moreau, S.; Perly, B.; Chachaty, C.; Deleuze, C. *Biochim. Biophys. Acta* **1985**, *840*, 107−116.

(25) Silver, J.; Lukas, B. *Inorg. Chim. Acta* **1983**, *78*, 219−224.

(26) Medhi, O. K.; Silver, J. *Inorg. Chim. Acta* **1988**, *153*, 133−134.

(27) Kuzelova, K.; Mrhalova, M.; Hrkal, Z. *Biochim. Biophys. Acta* **1997**, *1336*, 497−501.

(28) Srinivas, V.; Rao, C. M. *Biochem. Int.* **1990**, *21*, 849−855.

(29) de Villiers, K. A.; Kaschula, C. H.; Egan, T. J.; Marques, H. M. *J. Biol. Inorg. Chem.* **2007**, *12*, 101−117.

(30) Asher, C.; de Villiers, K. A.; Egan, T. J. *Inorg. Chem.* **2009**, *48*, 7994−8003.

(31) Crespo, M. P.; Tilley, L.; Klonis, N. *J. Biol. Inorg. Chem.* **2010**, *15*, 1009−1022.

(32) Casabianca, L. B.; An, D.; Natarajan, J. K.; Alumasa, J. N.; Roepe, P. D.; Wolf, C.; de Dios, A. C. *Inorg. Chem.* **2008**, *47*, 6077−6081.

(33) Kuter, D.; Benjamin, S. J.; Egan, T. J. *J. Inorg. Biochem.* **2014**, *133*, 40−49.

(34) Brooks, B. R.; Brooks, C. L., III; MacKerell, A. D., Jr.; Nilsson, L.; Petrella, R. J.; Roux, B.; Won, Y.; Archontis, G.; Bartels, C.; Boresch, S.; Caflisch, A.; Caves, L.; Cui, Q.; Dinner, A. R.; Feig, M.; Fischer, S.; Gao, J.; Hodoscek, M.; Im, W.; Kuczera, K.; Lazaridis, T.; Ma, J.; Ovchinnikov, V.; Paci, E.; Pastor, R. W.; Post, C. B.; Pu, J. Z.; Schaefer, H. F.; Tidor, B.; Veneble, R. M.; Woodcock, H. L.; Wu, X.; Yang, W.; York, D. M.; Karplus, M. *J. Comput. Chem.* **2009**, *30*, 1545−1614.

(35) Autenrieth, F.; Tajkhorshid, E.; Baudry, J.; Luthey-Schulten, Z. *J. Comput. Chem.* **2004**, *25*, 1613−1622.

(36) Horn, H. W.; Swope, W. C.; Pitera, J. W.; Madura, J. D.; Dick, T. J.; Hura, G. L.; Head-Gordon, T. *J. Chem. Phys.* **2004**, *120*, 9665−9678.

(37) Kuter, D.; Venter, G. A.; Naidoo, K. J.; Egan, T. J. *Inorg. Chem.* **2012**, *51*, 10233−10250.

(38) Ravel, B.; Newville, M. *J. Synchrotron Radiat.* **2005**, *12*, 537−541.

(39) Newville, M. *J. Synchrotron Radiat.* **2001**, *8*, 322−324.

(40) Ankudinov, A. L.; Nesvizhskii, A. I.; Rehr, J. J. *Phys. Rev. B* **2003**, *67*, 115120.

(41) Stern, E. A. *Phys. Rev. B* **1993**, *48*, 9825−9827.

(42) Cheng, L.; Lee, J.; Powell, D. R.; Richter-Addo, G. B. *Acta Crystallogr.* **2004**, *E60*, m1340−1342.

(43) Hudson, E. A.; Allen, P. G.; Terminello, L. J. *Phys. Rev. B* **1996**, *54*, 156−165.

(44) Karolewski, M. A.; Cavell, R. G.; Gordon, R. A.; Glover, C. J.; Cheah, M.; Ridgway, M. C. *J. Synchrotron Radiat.* **2013**, *20*, 555−566.

(45) Provost, K.; Beret, E. C.; Bouvet Muller, D.; Michalowicz, A.; Sànchez Marcos, E. *J. Chem. Phys.* **2013**, *138*, 084303.

(46) *Cambridge Structural Database and Cambridge Structrural Database System*, version 1.13; Cambridge Crystallographic Data Centre, University Chemical Laboratory: Cambridge, 2011.

(47) de Hatten, X.; Cournia, Z.; Huc, I.; Smith, J. C.; Metzler-Nolte, N. *Chem.—Eur. J.* **2007**, *13*, 8139−8152.

(48) Naidoo, K. J.; Klatt, G.; Koch, K. R.; Robinson, D. J. *Inorg. Chem.* **2002**, *41*, 1845−1849.

(49) Frisch, M. J.; Trucks, G. W.; Schlegel, H. B.; Scuseria, G. E.; Robb, M. A.; Cheeseman, J. R.; Scalmani, G.; Barone, V.; Mennucci, B.; Petersson, G. A.; Nakatsuji, H.; Caricato, M.; Li, X.; Hratchian, H. P.; Izmaylov, A. F.; Bloino, J.; Zheng, G.; Sonnenberg, J. L.; Hada, M.; Ehara, M.; Toyota, K.; Fukuda, R.; Hasegawa, J.; Ishida, M.; Nakajima, T.; Honda, Y.; Kitao, O.; Nakai, H.; Vreven, T.; Montgomery, J. A. J.; Peralta, J. E.; Ogliaro, F.; Bearpark, M.; Heyd, J. J.; Brothers, E.; Kudin, K. N.; Staroverov, V. N.; Kobayashi, R.; Normand, J.; Raghavachari, K.; Rendell, A.; Burant, J. C.; Iyengar, S. S.; Tomasi, J.; Cossi, M.; Rega, N.; Millam, N. J.; Klene, M.; Knox, J. E.; Cross, J. B.; Bakken, V.; Adamo, C.; Jaramillo, J.; Gomperts, R.; Stratmann, R. E.; Yazyev, O.; Austin, A. J.; Cammi, R.; Pomelli, C.; Ochterski, J. W.; Martin, R. L.; Morokuma, K.; Zakrzewski, V. G.; Voth, G. A.; Salvador, P.; Dannenberg, J. J.; Dapprich, S.; Daniels, A. D.; Farkas, Ö.; Foresman, J. B.; Ortiz, J. V.; Cioslowski, J.; Fox, D. J. *Gaussian 09*; Gaussian Inc.: Wallington, 2009.

(50) Nosé, S. *Mol. Phys.* **1984**, *52*, 255−268.

(51) Hoover, W. G. *Phys. Rev. A* **1984**, *31*, 1695−1697.

(52) Feller, S. E.; Zhang, Y.; Pastor, R. W.; Brooks, B. R. *J. Chem. Phys.* **1995**, *103*, 4613−4621.

(53) Matthews, R. P.; Venter, G. A.; Naidoo, K. J. *J. Phys. Chem. B* **2011**, *115*, 1045−1055.

(54) Naidoo, K. J.; Kuttel, M. *J. Comput. Chem.* **2001**, *22*, 445−456.

(55) Best, R. B.; Jackson, G. E.; Naidoo, K. J. *J. Phys. Chem. B* **2001**, *105*, 4742−4751.

(56) Scheidt, W. R.; Lee, Y. J. *Struct. Bonding (Berlin)* **1987**, *64*, 1−70.

(57) Cuya Guizado, T. R.; Louro, S. R. W.; Anteneodo, C. *J. Chem. Phys.* **2011**, *134*, 055103.

(58) Laaksonen, A.; Stilbs, P.; Wasylishen, R. E. *J. Chem. Phys.* **1998**, *108*, 455−468.

(59) Binsted, N.; Strange, R. W.; Hasnain, S. S. *Biochemistry* **1992**, *31*, 12117−12125.

(60) Dziedzic-Kocurek, K.; Stanek, J.; Burda, K. *Hyperfine Interact.* **2008**, *185*, 87−93.

(61) Dziedzic-Kocurek, K.; Okła, D.; Stanek, J. *Nukleonika* **2013**, *58*, 7−11.

(62) Slater, A. F. G.; Swiggard, W. J.; Orton, B. R.; Flitter, W. D.; Goldberg, D. E.; Cerami, A.; Henderson, G. B. *Proc. Natl. Acad. Sci. U.S.A.* **1991**, *88*, 325−329.

(63) Walczak, M.; Lawniczak-Janlonska, K.; Sienkiewicz, A.; Demchenko, I. N.; Piskorska, E.; Chatain, G.; Bohle, D. S. *Nucl. Instrum. Methods Phys. Res., Sect. B* **2005**, *238*, 32−38.

(64) Walczak, M. S.; Lawniczak-Jablonska, K.; Sienkiewicz, A.; Klepka, M. T.; Suarez, L.; Kosar, A. J.; Bellemare, M.-J.; Bohle, D. S. *J. Non-Cryst. Solids* **2010**, *356*, 1908−1913.

(65) Walczak, M. S.; Lawniczak-Jablonska, K.; Wolska, A.; Sienkiewicz, A.; Suárez, L.; Kosar, A. J.; Bohle, D. S. *J. Phys. Chem. B* **2011**, *115*, 1145−1150.

(66) Walczak, M. S.; Lawniczak-Jablonska, K.; Wolska, A.; Sikora, M.; Sienkiewicz, A.; Suárez, L.; Kosar, A. J.; Bellemare, M.-J.; Bohle, D. S. *J. Phys. Chem. B* **2011**, *115*, 4419−4426.

(67) Lee, H. M.; Olmstead, M. M.; Gross, G. G.; Balch, A. L. *Cryst. Growth Des.* **2003**, *3*, 691−697.

(68) Ghosh, S. K.; Patra, R.; Rath, S. P. *Inorg. Chem.* **2008**, *47*, 10196−10198.

(69) Ghosh, S. K.; Patra, R.; Rath, S. P. *Inorg. Chim. Acta* **2010**, *363*, 2791−2799.

(70) Deng, Y.; Chang, C. J.; Nocera, D. G. *J. Am. Chem. Soc.* **2000**, *122*, 410−411.

(71) Landrum, J. T.; Grimmett, D.; Haller, K. J.; Scheidt, W. R.; Reed, C. A. *J. Am. Chem. Soc.* **1981**, *103*, 2640−2650.

(72) Lay, K. L.; Buchler, J. W.; Kenny, J. E.; Scheidt, W. R. *Inorg. Chim. Acta* **1986**, *123*, 91−97.

(73) Scheidt, W. R.; Cheng, B.; Safo, M. K.; Cukiernik, F.; Marchon, J.-C.; Debrunner, P. G. *J. Am. Chem. Soc.* **1992**, *114*, 4420−4421.

(74) Evans, D. R.; Mathur, R. S.; Heerwegh, K.; Reed, C. A.; Xie, Z. *Angew. Chem., Int. Ed.* **1997**, *36*, 1335−1337.

(75) Ghosh, S. K.; Rath, S. P. *J. Am. Chem. Soc.* **2010**, *132*, 17983−17985.

(76) Chen, Z.; Xu, Z.; Zhang, L.; Yan, F.; Lin, Z. *J. Phys. Chem. A* **2001**, *105*, 9710−9716.

(77) Egan, T. J.; Chen, J. Y.-J.; de Villiers, K. A.; Mabotha, T. E.; Naidoo, K. J.; Ncokazi, K. K.; Langford, S. J.; McNaughton, D.; Pandiancherri, S.; Wood, B. R. *FEBS Lett.* **2006**, *580*, 5105−5110.

(78) Reedy, C. J.; Gibney, B. R. *Chem. Rev.* **2004**, *104*, 617−649.